Cellular Oncology (2025) 48:709–723
https://doi.org/10.1007/s13402-025-01041-0

RESEARCH

Predicting the early therapeutic response to hepatic artery infusion chemotherapy in patients with unresectable HCC using a contrast-enhanced computed tomography-based habitat radiomics model: a multi-center retrospective study

Mingsong Wu[1] · Zenglong Que[2] · Shujie Lai[1] · Guanhui Li[1] · Jie Long[1] · Yuqin He[1] · Shunan Wang[3] · Hao Wu[4] · Nan You[5] · Xiang Lan[6] · Liangzhi Wen[1]

Accepted: 23 January 2025 / Published online: 4 February 2025
© The Author(s) 2025

Abstract

Objective Predicting the therapeutic response before initiation of hepatic artery infusion chemotherapy (HAIC) with fluorouracil, leucovorin, and oxaliplatin (FOLFOX) remains challenging for patients with unresectable hepatocellular carcinoma (HCC). Herein, we investigated the potential of a contrast-enhanced CT-based habitat radiomics model as a novel approach for predicting the early therapeutic response to HAIC-FOLFOX in patients with unresectable HCC.

Methods A total of 148 patients with unresectable HCC who received HAIC-FOLFOX combined with targeted therapy or immunotherapy at three tertiary care medical centers were enrolled retrospectively. Tumor habitat features were extracted from subregion radiomics based on CECT at different phases using k-means clustering. Logistic regression was used to construct the model. This CECT-based habitat radiomics model was verified by bootstrapping and compared with a model based on clinical variables. Model performance was evaluated using the area under the curve (AUC) and a calibration curve.

Results Three intratumoral habitats with high, moderate, and low enhancement were identified to construct a habitat radiomics model for therapeutic response prediction. Patients with a greater proportion of high-enhancement intratumoral habitat showed better therapeutic responses. The AUC of the habitat radiomics model was 0.857 (95% CI: 0.798–0.916), and the bootstrap-corrected concordance index was 0.842 (95% CI: 0.785–0.907), resulting in a better predictive value than the clinical variable-based model, which had an AUC of 0.757 (95% CI: 0.679–0.834).

Conclusion The CECT-based habitat radiomics model is an effective, visualized, and noninvasive tool for predicting the early therapeutic response of patients with unresectable HCC to HAIC-FOLFOX treatment and could guide clinical management and decision-making.

Keywords Liver · Unresectable hepatocellular carcinoma · Hepatic artery infusion chemotherapy · Response to treatment · Habitat radiomics

Abbreviations

HCC	Hepatocellular carcinoma
AUC	Area under the curve
AP	Arterial phase
AE	Arterial enhancement
APHE	Arterial phase hyperenhancement
BCLC	Barcelona Clinical Liver Cancer
CECT	Contrast-enhanced computed tomography
CI	Confidence interval
CTP	Child-Turcotte-Pugh
DSA	Digital subtraction angiography
FOLFOX	Oxaliplatin plus fluorouracil and leucovorin
HAIC	Hepatic arterial infusion chemotherapy
ICC	Intraclass correlation coefficient

Mingsong Wu, Zenglong Que and Shujie Lai contribute equally to this work.

Extended author information available on the last page of the article

LI-RADS	Liver Imaging Reporting and Data System
mRECIST	Modified Response Evaluation Criteria for Solid Tumors
MRI	Magnetic resonance imaging
MSI	Multiregional spatial interaction
MVI	Microvascular invasion
OR	Odds ratio
ORR	Objective response rate
OS	Overall survival
PFS	Progression-free survival
TACE	Transarterial chemoembolization
PVP	Portal venous phase
ROC	Receiver operating characteristic
ROI	Region of interest
TKIs	Tyrosine kinase inhibitors
VE	Venous Phase Enhancement
VP	Vascular invasion vp classification

1 Introduction

Hepatocellular carcinoma (HCC), the main pathological type of primary liver cancer, is one of the most common malignant tumors, with the sixth highest incidence and third highest mortality rate worldwide [1]. Due to the insidious onset of HCC, less than 10% of patients are eligible for curative resection at the time of diagnosis [2]. Approximately 40-50% of patients are diagnosed at intermediate or advanced stages [3], making curative resection impossible, and the median survival time is only a few months [4, 5]. Currently, hepatic arterial infusion chemotherapy (HAIC) based on oxaliplatin, calcium folinate, and fluorouracil (FOLFOX) has been incorporated into the standard treatment for unresectable HCC in most Asian countries [6–10]. Although HAIC-FOLFOX significantly improved overall survival (23.1 vs. 16.1 months) of patients with unresectable HCC compared with transarterial chemoembolization (TACE), its therapeutic response rate is only 46% [11]. Therefore, identifying suitable candidates for HAIC-FOLFOX treatment is highly valuable for guiding clinical decision-making in managing patients with unresectable HCC.

However, the prediction of HAIC-FOLFOX efficacy in patients with unresectable HCC is challenging owing to high tumor heterogeneity and different sensitivities to chemotherapeutic agents [12]. Currently reported prediction models include serologic indicators (AFP, ABLI, NLP, etc.), clinical staging (Child–Pugh classification, BCLC staging, or AJCC staging), and CT- and magnetic resonance imaging (MRI)-based radiomics. Serologic indicators and clinical staging have limited predictive value due to marked individual variation. Additionally, traditional radiomics, which calculates features across the entire tumor, has limitations because it overlooks the heterogeneity within tumor subregions and does not allow interpretation of the extensive features extracted.

In contrast to traditional radiomics, habitat radiomics characterizes tumors by dividing them into different subregions, termed habitats, and visualizing the compositional components of the tumor and differences in spatial distribution among subregions, thereby elucidating tumor composition and interactions within the tumor microenvironment [13]. Tumor habitat radiomics has been widely used as a new imaging approach to predict the prognosis of patients with locally advanced breast cancer and the recurrence of hepatocellular carcinoma (≤5 cm) after surgical resection [14, 15]. This image-based intratumoral partitioning allows the intuitive quantification of the tumor composition and spatial interactions, by identifying subregions or components that are most relevant to tumor biological behavior and invasiveness.

However, whether habitat radiomics could be a useful tool for predicting the prognosis of patients with unresectable HCC after HAIC-FOLFOX treatment has not been reported. Since the high rate of drug resistance after multiple HAIC-FOLFOX treatments and the first response to interventional therapy strongly correlates with prognosis and survival [16, 17], we focused on the early therapeutic response to HAIC-FOLFOX treatment. Contrast-enhanced computed tomography (CECT) scans are cost-effective and widely accessible, making them one of the recommended standard methods for diagnosing and monitoring HCC according to the Liver Imaging Reporting and Data System (LI-RADS) guidelines. The present study aimed to construct a CECT-based intratumoral habitat radiomics model to predict the early therapeutic response of patients with unresectable HCC to HAIC-FOLFOX.

2 Materials and methods

2.1 Study design

Ethical approval for this retrospective multicenter study was obtained from three centers. The flowchart of the study design is shown in Fig. 1a. Between October 2021 and October 2024, 1,135 HCC patients who underwent HAIC-FOLFOX were screened at three hospitals. HCC was diagnosed according to the American Association for the Study of Liver Diseases (AASLD) guidelines. Based on the inclusion and exclusion criteria, 148 patients with HCC were ultimately included. Among all patients, a total of 77 patients underwent TKIs and 120 patients underwent PD-1 therapy after HAIC.

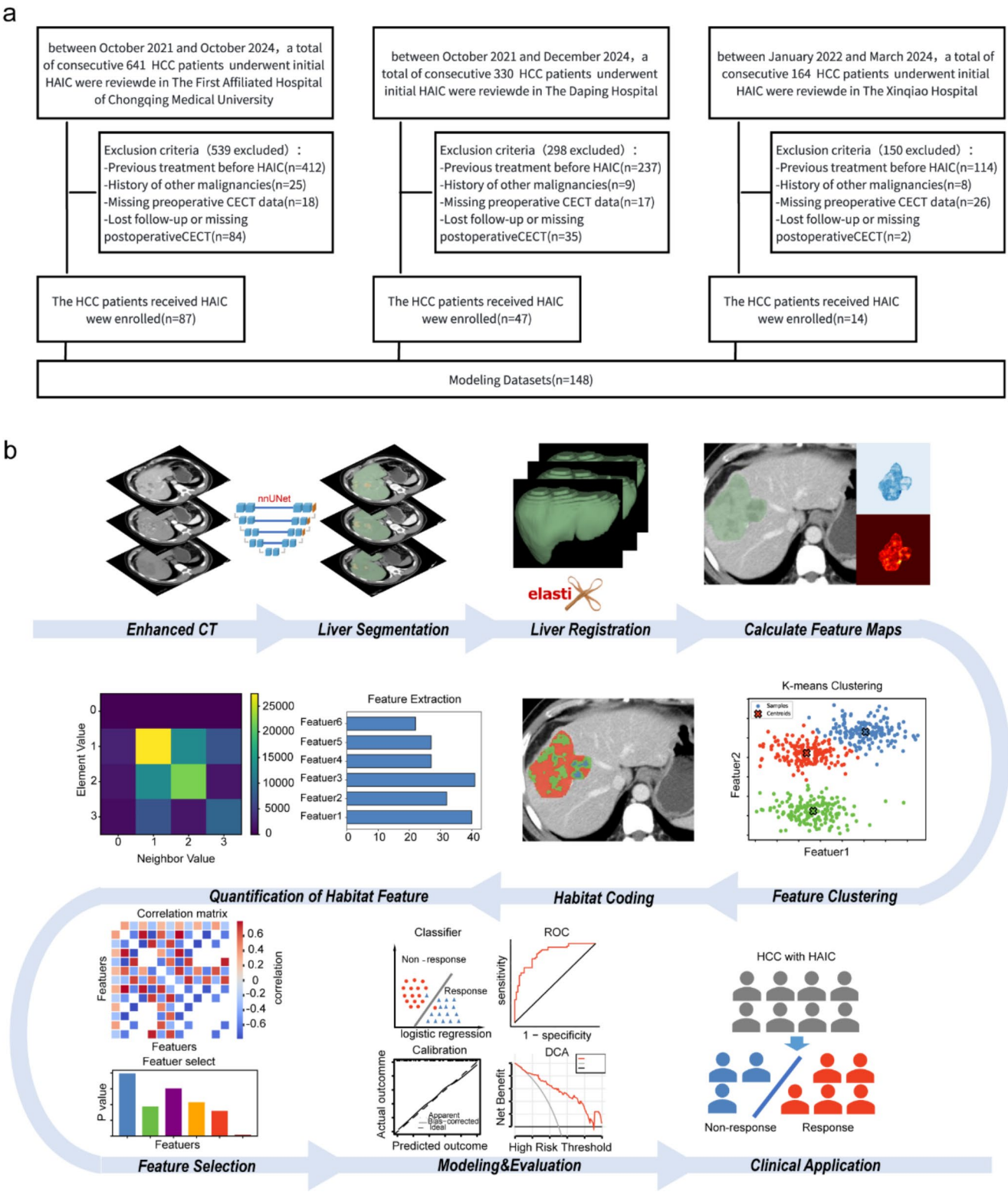

Fig. 1 Study design for building a habitat radiomics model to predict HAIC-FOLFOX response in unresectable HCC

2.2 Follow-up and response assessment

All patients were followed up until the last recorded follow-up date (1 December 2024). The response to HAIC-FOLFOX was evaluated based on CECT images obtained 1 to 2 months after the completion of the two HAIC-FOLFOX treatments according to the modified Response Evaluation Criteria in Solid Tumors (mRECIST) [18]. All patients were divided into an objective response (OR = PR + CR) group and a non-OR (nOR = SD + PD) group. Two radiologists, each with more than 8 years of experience in abdominal imaging, assessed the OR without knowledge of the clinical procedures. In cases of conflicting interpretations, a final consensus was reached through discussion.

2.3 CECT screening protocols

CECT scans were performed using a SOMATOM Perspective (Siemens Healthineers, Erlangen, Germany), SOMATOM Definition Flash (Siemens Healthineers, Erlangen, Germany), or Discovery CT750 HD (GE Healthcare, Milwaukee, WI, USA) CECT scanner following a standardized protocol. A three-phase scan (plain, arterial phase, and venous phase scan) was performed on each patient. The CECT scanning parameters were as follows: tube voltage, 100 kV; the tube current, 75 mA; and the slice thickness, 1–5 mm. Images were reconstructed as axial images using a B60f filter with a slice thickness of 1 mm and a slice increment of 1 mm. CECT images were obtained after intravenous administration of iohexol (300 mg/mL at a rate of 3.0 mL/s, followed by a 30-mL saline flush). Arterial phase scanning was initiated 10–15 s after reaching a trigger threshold (100 Hu) in the abdominal aorta, and portal venous phase scanning was conducted 30–35 s after the end of the arterial phase. The total contrast volume was 1.5 mL/kg.

2.4 Image analysis

In this study, HCC habitat imaging consisted of the following four primary technical stages: image preprocessing, tumor segmentation, habitat encoding, and habitat feature extraction.

2.5 Image preprocessing

All images were first discretized by setting the bin count to 256 to normalize the intensity and reduce image noise, and then resampled to $1 \times 1 \times 1$ mm to normalize voxel spacing. Using nnUNet (https://zenodo.org/record/3734294#.XyYR5mMzY5n), a pretrained liver segmentation model, the liver region underwent three successive stages of division. The evaluation was conducted by Reader 1 (W.M.S., a physician with five years of experience in abdominal imaging) and manually adjusted for inadequate masking. Subsequently, the Elastix software (5.1.0-win64 https://elastix.dev/) was used with registration parameter packs (Par0057Bspline, https://github.com/SuperElastix/ElastixModelZoo/tree/master/models). The liver region in the portal vein phase image served as the reference mask, while the liver regions in other images underwent B-spline transformation [19].

2.6 Tumor segmentation

The portal vein phase CT images were imported into the open-source 3D Slicer software (version 5.2.2, www.slicer.org). Two experienced radiologists carefully delineated the boundaries of the lesions layer by layer to generate 2D regions of interest (ROIs). For cases with multiple nodules, the two largest lesions, each with a diameter greater than 2 cm, were selected as the target lesions. Following this, three-dimensional regions of interest (3D ROIs) were automatically generated from the 2D ROIs of the intrahepatic lesions. Given the alignment of the scanning and arterial phase images with the venous phase image, the obtained tumor ROIs were also synchronized with other temporal images.

2.7 Habitat encoding

We obtained two parametric maps, an arterial phase enhancement (AE) map (Fig. 2a) and a venous phase enhancement (VE) map (Fig. 2b). The mathematical definitions of AE and VE are as follows:

$$AE = CT_{AP} - CT_{Pre} \qquad VE = CT_{VP} - CT_{Pre}$$

where CT stands for computed tomography attenuation values, measured in Hounsfield units (Hu). AP represents the arterial phase, VP represents the portal venous phase, and Pre represents the pre-enhancement phase.

As the AE and VE maps are coregistered, each voxel within the tumor ROI corresponds to both an AE and VE value. By aggregating voxels from all the ROIs, feature vectors containing AE and VE signals are formed. K-means clustering [14] (implemented using the scikit-learn 1.0.2 package in Python) was then employed to group these feature vectors into habitats. The range of candidate clusters was tested from 2 to 15, with both the elbow method and silhouette coefficient used to determine the optimal number of clusters [20].

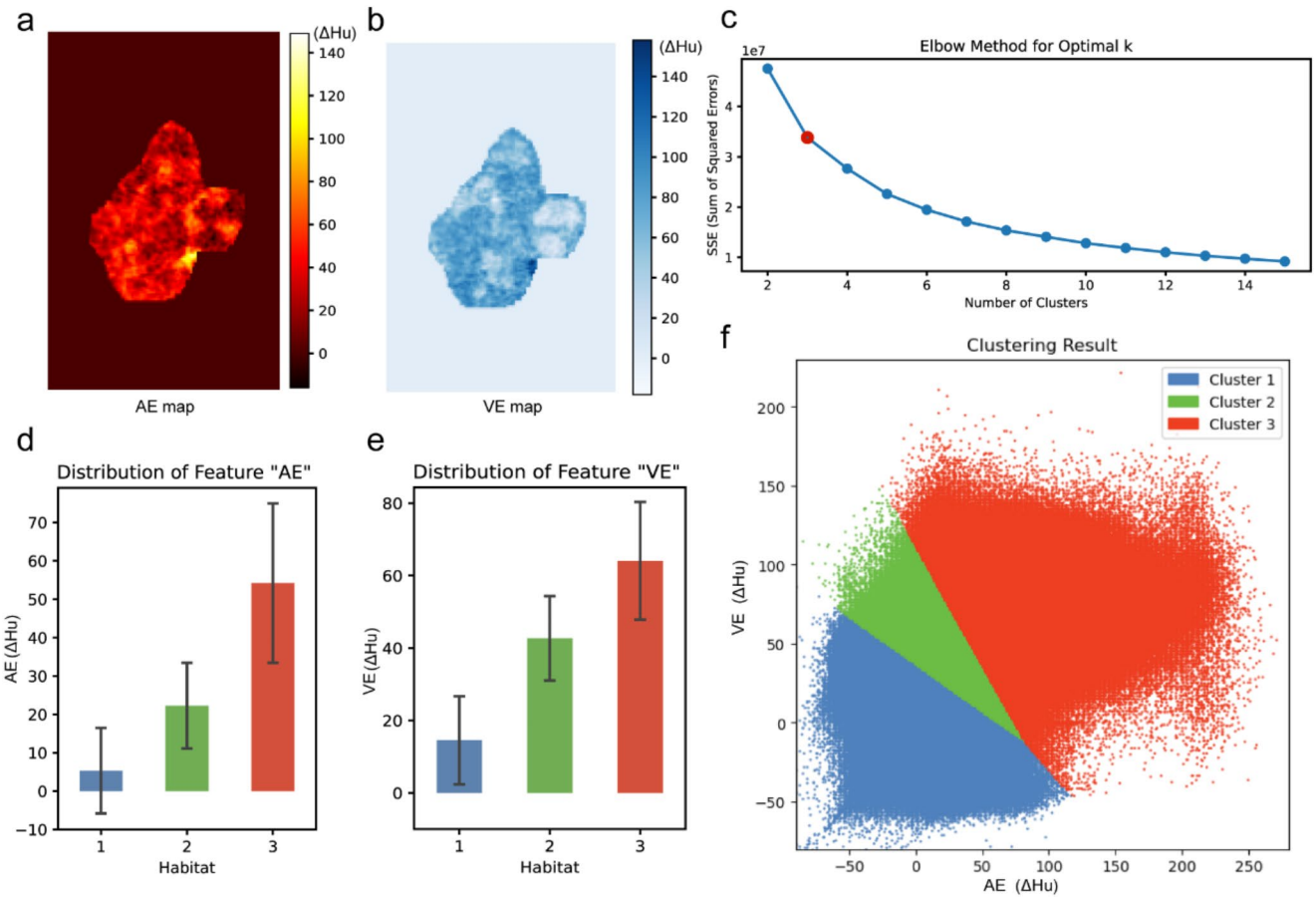

Fig. 2 Features used to encode habitats and their distribution. (**a**) "AE" and (**b**) "VE" parametric maps used to encode habitats; (**c**) Elbow rule used to determine the optimal number of clusters; Features of "AE" (**d**) and "VE" (**e**) distribution bar chart of each habitat subregion; (**f**) Scatter plot of characteristic distribution in each habitat subregion

2.8 Habitat feature extraction

Intratumoral spatial heterogeneity was characterized and quantified through a multiregional spatial interaction (MSI) matrix, which retrieves neighboring pairs for each tumor voxel and subsequently adds them to the corresponding entry in the MSI matrix (Fig. 3a and b). All voxels underwent classification, and the spatial heterogeneity was summarized within the final MSI matrix. A comprehensive set of 34 features, comprising 30 first-order and four second-order statistical features, was derived from the MSI matrix [14]. Additionally, features were calculated for the number of habitat voxels, including the habitat volume and its proportions. These analyses collectively elucidated the extent of spatial heterogeneity within the tumor.

We evaluated the stability of the extracted features by conducting intra- and interreader reproducibility assessments. For this purpose, Reader 1 outlined the tumor ROIs twice within a one-week interval for 30 randomly selected patients, while Reader 2 (Q.Z.L.) independently performed segmentation. Intraclass correlation coefficients (ICCs) were calculated to assess reproducibility. Habitat features with intra- and interobserver ICCs > 0.8 were chosen for subsequent analysis. Additionally, features categorized by efficacy were subjected to t-tests/Mann–Whitney U tests, and those with a p-value less than 0.05 were retained. The remaining features were paired two-by-two, and Spearman's correlation coefficients were computed. The feature with the most significant p-value from pairs with correlation coefficients exceeding 0.95 was retained. Dimensionality reduction of the retained features was performed using cross-validation with Lasso regression.

2.9 Model construction

Imaging features identified through screening were integrated into the modeling process. Bicategorical logistic regression was used to construct the habitat radiomics model. Initial screening of clinical characteristics involved univariate logistic regression to calculate odds ratios (ORs) and corresponding p-values. Variables with p-values less than 0.1 were then included in the multivariate stepwise

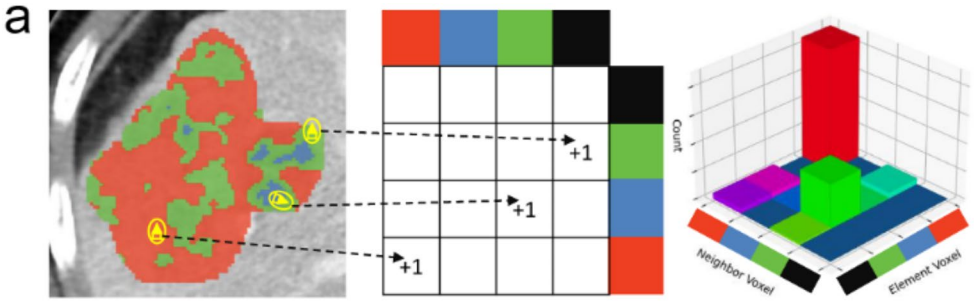

b

Type of Image Features	N	Interpretation
1st-order,absolute counts based on MSI matrix and tumor ROI	12	Volume of each subregion and borders of two differing subregions; Volume of sub regions based on voxel calculation
1st-order,relative counts based on normalized MSI matrix	25	Proportion of each subregion and borders of two differing subregions; The proportion of adjacent boundaries in paired sub regions to all boundaries in that sub region
2nd-order : contrast, homogeneity, energy, and entropy based on MSI matrix	4	Summary statistics of spatial heterogeneity of intratumor subregion maps

Fig. 3 Habitat features extraction. (**a**) The Illustration shows the use of a multiregional spatial interaction (MSI) matrix derived from intratumor habitat maps. (**b**) Forty-one quantitative imaging features were extracted to measure intratumoral spatial heterogeneity

logistic regression analysis. A combined model was formulated by incorporating the habitat model with clinically relevant variables identified through multifactorial screening.

2.10 Statistical analysis

Continuous variables are reported as either means with standard deviations (SD) or medians with interquartile ranges (IQRs), while categorical variables are presented as counts and percentages. The discriminative capacity of the models was assessed through receiver operating characteristic (ROC) curve analysis, calibration plots, and confusion matrices. Model validation was performed internally using 1,000 bootstrap samples with replacement, providing estimates of the area under the curve (AUC) and the associated 95% confidence interval (CI). Furthermore, model calibration and decision curve analyses were conducted to assess model performance. Computational implementation was performed using Python (version 3.7.6; https://www.python.org/) and the R software version 4.2.3 (http://www.r-project.org/). Statistical significance was set at a two-sided alpha level of 0.05.

3 Results

3.1 Patient cohort

Among 1,135 patients who were treated with HAIC-FOLFOX for HCC, 763 were excluded from this study owing to pretreatment, 42 were excluded owing to concurrent malignancies, and 61 were excluded owing to poor image quality or unclear images, and 121 were excluded owing to missing follow-up data (Fig. 1a). Finally, a total of 148 patients were enrolled in the study, with a mean age of 56 (±10.7) years, including 126 males and 22 females. The majority of patients (121 out of 148, 81.8%) presented with hepatitis B virus infection, and 105 patients (70.9%) had cirrhosis. According to BCLC staging system, 121 patients (81.8%) were classified as stage C. The median tumor diameter was 9.6 cm (range: 7.3–12.7 cm), and the objective response rate (ORR) of HAIC-FOLFOX was 52.7%. Among the cohort, 77 patients (52%) received with tyrosine kinase inhibitor (TKI) treatment, and 120 patients (81.1%) were administered programmed cell death protein 1 (PD-1) inhibitors. Further clinical details can be found in Table 1.

3.2 Habitat imaging and feature extraction

The research roadmap is illustrated in Fig. 1b. Tumor habitats were delineated through CT image preprocessing, tumor segmentation, feature map calculation, and clustering. Based on the elbow method and silhouette coefficient, k=3 was chosen as the number of habitats, and all tumor voxels were clustered into one of the three habitats (Fig. 2c and f). The AE and VE values of the three habitats were as follows: Habitat 1, AE=21.786±11.567, VE=43.429±12.314; Habitat 2, AE=22.269±11.159, VE=42.694±11.675; and Habitat 3, AE=54.206±20.778, VE=64.086±16.246 (Fig. 2d and e). We thus concluded that Habitats 1, 2, and 3

Table 1 Baseline characteristics of patients with unresectable HCC undergoing HAIC

Features	Level	Overall ($n=148$)
Gender (%)	Male	126 (85.1)
	Female	22 (14.9)
Age (mean (SD))		56.47 (10.76)
BMI (mean (SD))		23.04 (2.76)
PS (%)	0	131 (88.5)
	1	17 (11.5)
Etiology (%)	HBV	118 (79.7)
	HCV	2 (1.4)
	Alcohol	11 (7.4)
	Others	17 (11.5)
Comorbidities (%)	Absence	115 (77.7)
	Presence	33 (22.3)
HBV (%)	Absence	27 (18.2)
	Presence	121 (81.8)
Cirrhosis (%)	Absence	43 (29.1)
	Presence	105 (70.9)
Ascites (%)	Absence	114 (77.0)
	Presence	34 (22.9)
CP grade (%)	A	121 (81.8)
	B	27 (18.2)
ALBI score (mean (SD))		-2.40 (0.46)
ALBI grader (%)	1	54 (36.7)
	2	91 (61.9)
	3	2 (1.4)
PALBI score (mean (SD))		-2.30 (0.36)
PALBI grade (%)	1	40 (27.0)
	2	76 (51.3)
	3	32 (21.6)
NLP (mean (SD))		3.95 (2.47)
PLR (mean (SD))		170.99 (102.62)
d_tumor, cm (median (IQR))		9.6 (7.3–12.7)
Number of tumors (%)	1	45 (30.4)
	≥2	103 (69.6)
Vascular invasion (%)	Absence	59 (39.9)
	Presence	89 (60.1)
VP (%)	0	59 (39.9)
	1	5 (3.4)
	2	13 (8.8)
	3	33 (22.3)
	4	38 (25.7)
Metastasis (%)	Absence	71 (48.0)
	Presence	77 (52.0)
BCLC (%)	B	27 (18.2)
	C	121 (81.8)
WBC, 10^9/L (mean (SD))		5.87 (2.22)
Neu, 10^9/L (mean (SD))		4.11 (1.86)
Ly, 10^9/L (mean (SD))		2.43 (15.28)
RBC, 10^12/L (mean (SD))		4.49 (0.78)
Hb, g/L (mean (SD))		134.31 (22.83)
PLT, 10^9/L (mean (SD))		182.89 (101.59)
AFP, ng/ml (median (IQR))		1340.5 (55.1–10868.8)
AFP400 (%)	Absence	55 (37.2)
	Presence	93 (62.8)
AST, U/L (mean (SD))		92.03 (75.84)
ALT, U/L (mean (SD))		56.58 (41.20)
Albumin, g/L (mean (SD))		38.00 (5.11)
ALP, U/L (mean (SD))		180.70 (130.36)
GGT, U/L (mean (SD))		247.29 (236.79)
CBIL, umol/L (mean (SD))		5.68 (5.11)
TBIL, umol/L (mean (SD))		20.58 (11.73)
PT, s (mean (SD))		13.63 (1.49)
INR (mean (SD))		1.11 (0.12)
Cre, umol/L (mean (SD))		66.74 (22.52)
Na^+, mmol/L (mean (SD))		138.89 (2.81)
K^+, mmol/L (mean (SD))		4.08 (0.40)
TKI (%)	Absence	71 (48.0)
	Presence	77 (52.0)
PD-1 (%)	Absence	28 (18.9)
	Presence	120 (81.1)
outcome (%)	nOR	70 (48.3)
	OR	78 (52.7)

Continuous variables were presented as mean±standard deviation (SD) or median with interquartile range and compared using the t-test or Mann-Whitney U test. In contrast, categorical variables were presented as frequencies with percentages and compared using the chi-squared test

AFP, α-fetoprotein; AFP400, α-fetoprotein over 400ng/ml; ALBI, albumin-bilirubin; ALT, alanine aminotransferase; ALP, alkaline phosphatase; AST, aspartate aminotransferase; BCLC, Barcelona Clinical Liver Cancer; BMI, body mass index; CBIL, conjugated bilirubin; Cre, creatinine; CP grade Child Pugh grade; d_tumor, tumor diameter; GGT, gamma glutamyl transferase; Hb, hemoglobin; HBV, viral hepatitis type B; HCV, viral hepatitis type C; INR, international normalized ratio; Ly, lymphocyte; Neu, Neutrophils; NLR, neutrophil to lymphocyte ratio; nOR, non objective response; OR, objective response. PALBI, platelet-albumin-bilirubin; PD-1, programmed death-1 inhibitor; PLR, platelet to lymphocyte ratio; PLT, platelet; PS, performance status; PT, prothrombin time; RBC, red blood cell; TBIL, total bilirubin; TKI, tyrosine kinase inhibitor; VP, vascular invasion vp classification; WBC, white blood cell

represented low-, moderate-, and high-perfusion subregions in the tumor, respectively. At the population level, the proportions of Habitats 1, 2, and 3 were 34.58%, 47.72%, and 17.70%, respectively. The spatial distribution of the habitats apparently varied between patients who responded well and those who responded poorly to the HAIC-FOLFOX treatment. Representative images of patients are shown in Fig. 4a and b. For habitat radiomic feature extraction, we quantified the spatial distribution of the habitats and the extent of their interactions using the MSI (Fig. 3a and b). Following the feature selection strategy, five key habitat radiomic features were ultimately selected for further analysis (Fig. 5a-d).

3.3 Modeling

The significant habitat features were selected, and a binary logistic regression was used to establish a habitat risk score, formulated as follows:

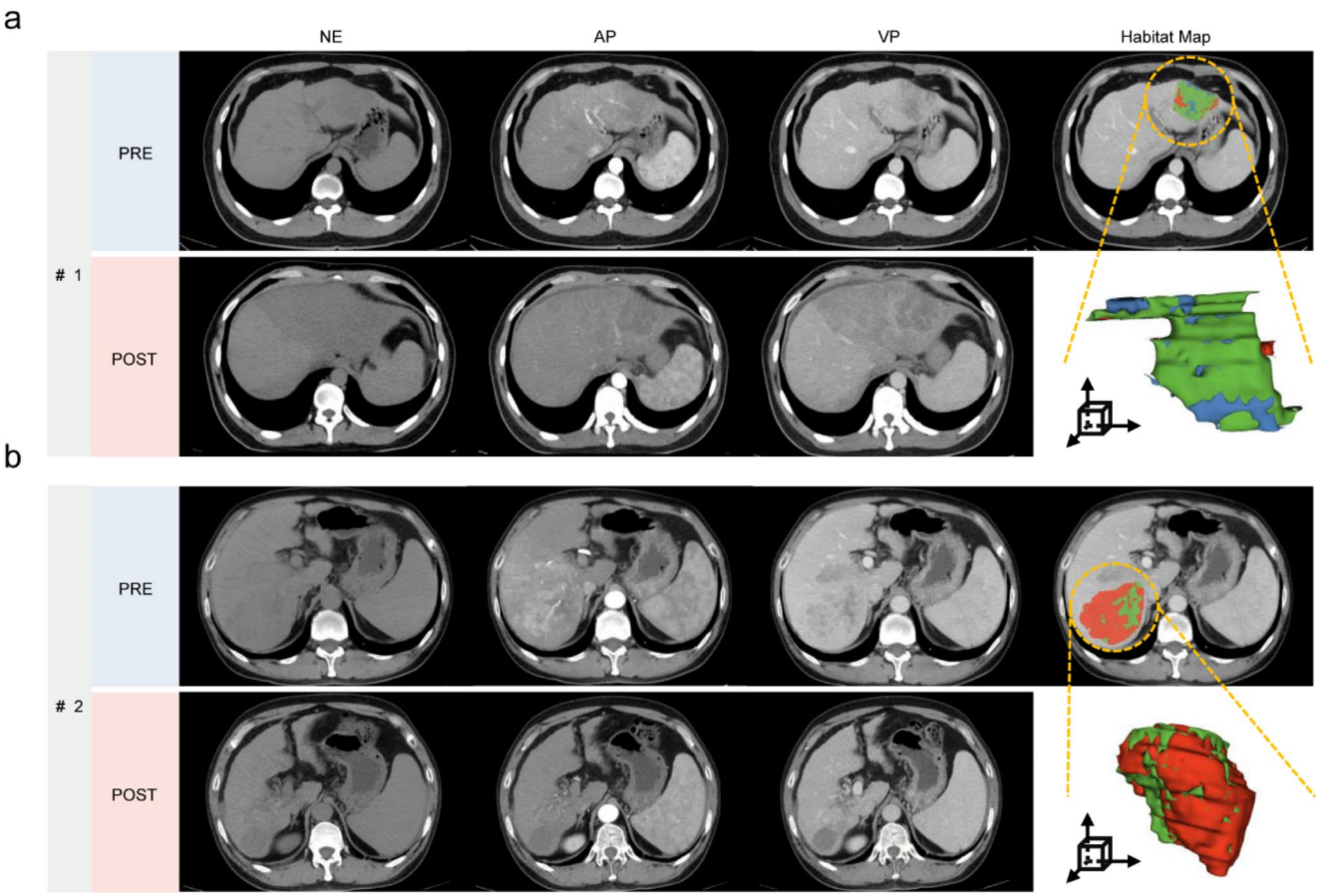

Fig. 4 Representative CECT images and habitat maps of two HCC patients. (**a**) CECT images of a nOR patient before and post treatment; (**b**) CECT images of a OR patient before and post treatment; The high enhancement subregion is in red, with moderate enhancement in green and low enhancement in blue

$$\begin{aligned} Habitat\ radiomics\ model = {} & 0.1689 + 0.0722 * (2b3r) \\ & + 0.7221 * (habitat3.1) \\ & - 0.6679 * (habitat1.1) \\ & - 0.5208 * (b01) + 0.7522 * (2border0) \end{aligned}$$

For clinical data analysis, indicators related to the response to HAIC-FOLFOX treatment are presented in Table 2. Logistic regression was used to construct a clinical score as follows:

$$\begin{aligned} Clinical\ model = {} & 1.9806 - 1.5059 * (Comorbidities) \\ & + 1.2923 * VP - 0.0470 * (TBIL) \\ & - 1.0785 * (Cirrhosis) \end{aligned}$$

The significant clinical indicators were combined with the habitat scores to construct a composite model, formulated as follows:

$$\begin{aligned} Combined\ model = {} & 1.8243 - 1.8950 * (Comorbidities) \\ & + 1.1727 * VP4 - 0.0442 * (TBIL) \\ & - 0.6937 * (Cirrhosis) + 1.0357 \\ & * (Habitat\ radiomics\ score) \end{aligned}$$

3.4 Performance evaluation

According to the ROC curve analysis, the areas under the curves (AUCs) for the habitat radiomics model, clinical model, and combined model were 0.857 (95% CI: 0.798–0.916), 0.757 (95% CI: 0.679–0.834), and 0.912 (95% CI: 0.861–0.963) respectively, as illustrated in Fig. 6a. The habitat radiomics model significantly outperformed the clinical model (P=0.033, DeLong test). Furthermore, the combined model also significantly outperformed the habitat radiomics model (P=0.004, DeLong test). To assess the stability and reliability of the model, we performed 1000 bootstrap resamples on the habitat radiomics model, and the calibration consistency index (C-index) of the habitat radiomics model was 0.842 (95% CI: 0.785–0.907). The calibration curve showed that the habitat radiomics model had high agreement between the predicted and actual probabilities. When the predicted probability falls between 0.4 and 0.8, the habitat radiomics model tends to overestimate the occurrence of treatment response (Fig. 6b). At a threshold probability of 0.5, the decision curve indicated that the combined

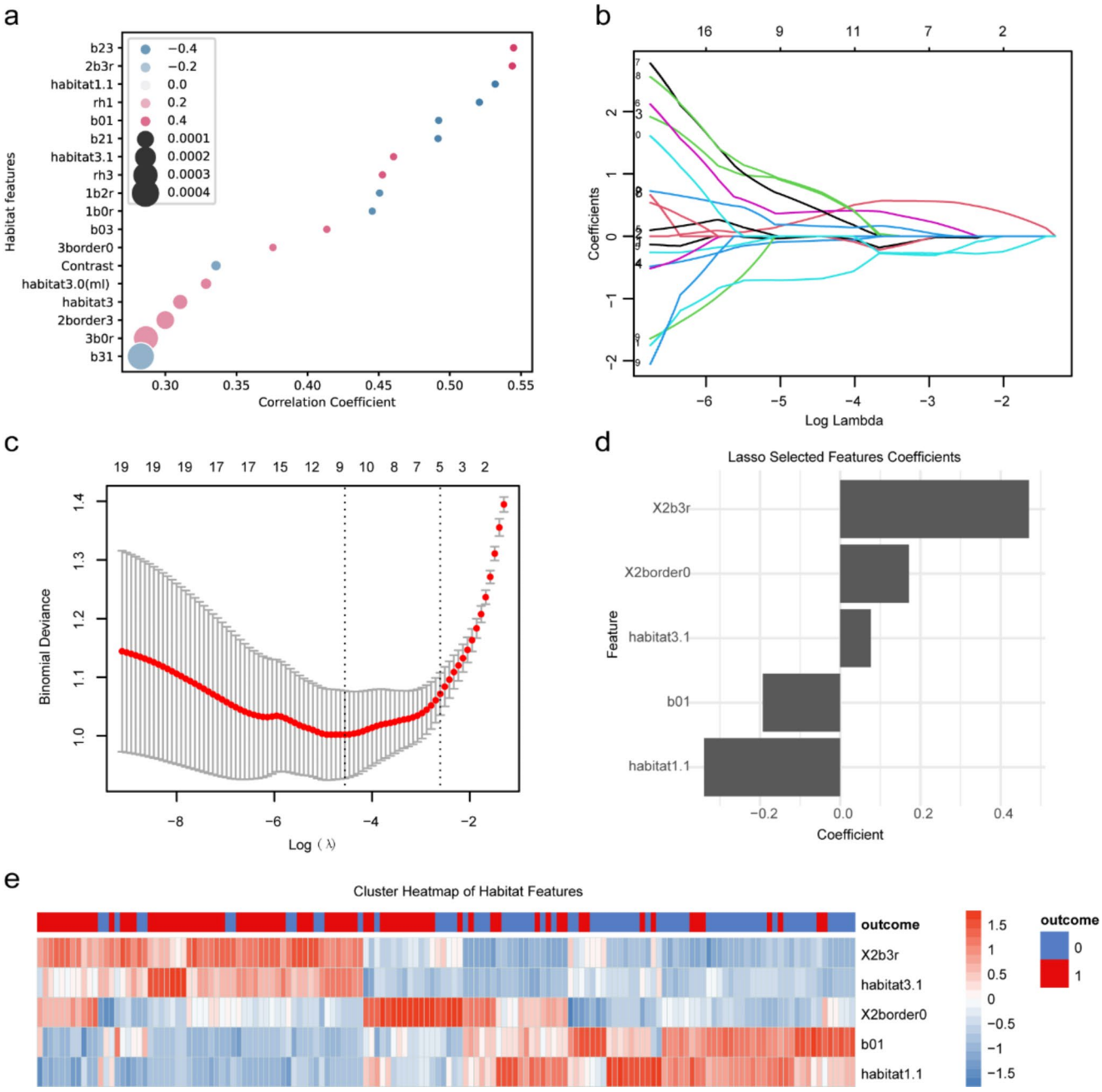

Fig. 5 Habitat features screening and clustering. (**a**) Bubble chart displaying the ranking of habitat features based on their importance; (**b**) and (**c**) Feature dimensionality reduction using Lasso regularization; (**d**) Features retained after Lasso dimensionality reduction; (**e**) Heatmap of hierarchical clustering of selected habitat features

model achieved the greatest net clinical benefit, followed by the habitat radiomics model (Fig. 6c). The radar chart provides a visual comparison of three models: evaluated across six metrics: AUC, accuracy, sensitivity, specificity, TPR, and TNR (Fig. 6d). The combined model outperforms the other two models consistently across all metrics, reflecting its comprehensive predictive performance. The habitat radiomics model outperforms the clinical model comprehensively. To further evaluate the classification ability of the habitat radiomics model, the confusion matrix demonstrated that the model achieved higher classification accuracy (Fig. 7a). There was a significant difference in the score distribution of the habitat radiomics model between the objective response group and the non-response group ($p<0.001$) (Fig. 7b). The alluvial diagram showed that the predictions of therapeutic outcomes by the habitat radiomics model were very close to the actual outcomes (Fig. 7c).

Table 2 Univariate and multivariate regression analysis of clinical variables

	Univariate			Multivariate		
	p	OR	CI	*p*	OR	CI
AFP>400	0.018	2.270	1.149–4.485			
Age	0.018	0.962	0.932–0.993			
Comorbidities	0.013	0.358	0.159–0.808	0.001	0.222	0.088–0.560
d_tumor(cm)	0.032	1.095	1.008–1.189			
PLT (10^9/L)	0.033	1.004	1-1.008			
TBIL (umol/L)	0.036	0.967	0.937–0.998	0.008	0.954	0.921–0.988
Cirrhosis	0.055	0.487	0.234–1.015	0.012	0.340	0.146–0.790
AST (U/L)	0.069	1.005	1-1.010			
VP	0.089	2.094	0.892–4.917	0.010	3.641	1.369–9.681

The clinical variables, screened through single-factor and multi-factor logistic regression, are presented as odds ratios, along with their corresponding 95% confidence intervals and associated *p*-values

AFP>400, α-fetoprotein over 400 ng/ml; AST, aspartate aminotransferase; d_tumor, tumor diameter; PLT, platelet; TBIL, total bilirubin; VP, vascular invasion vp classification

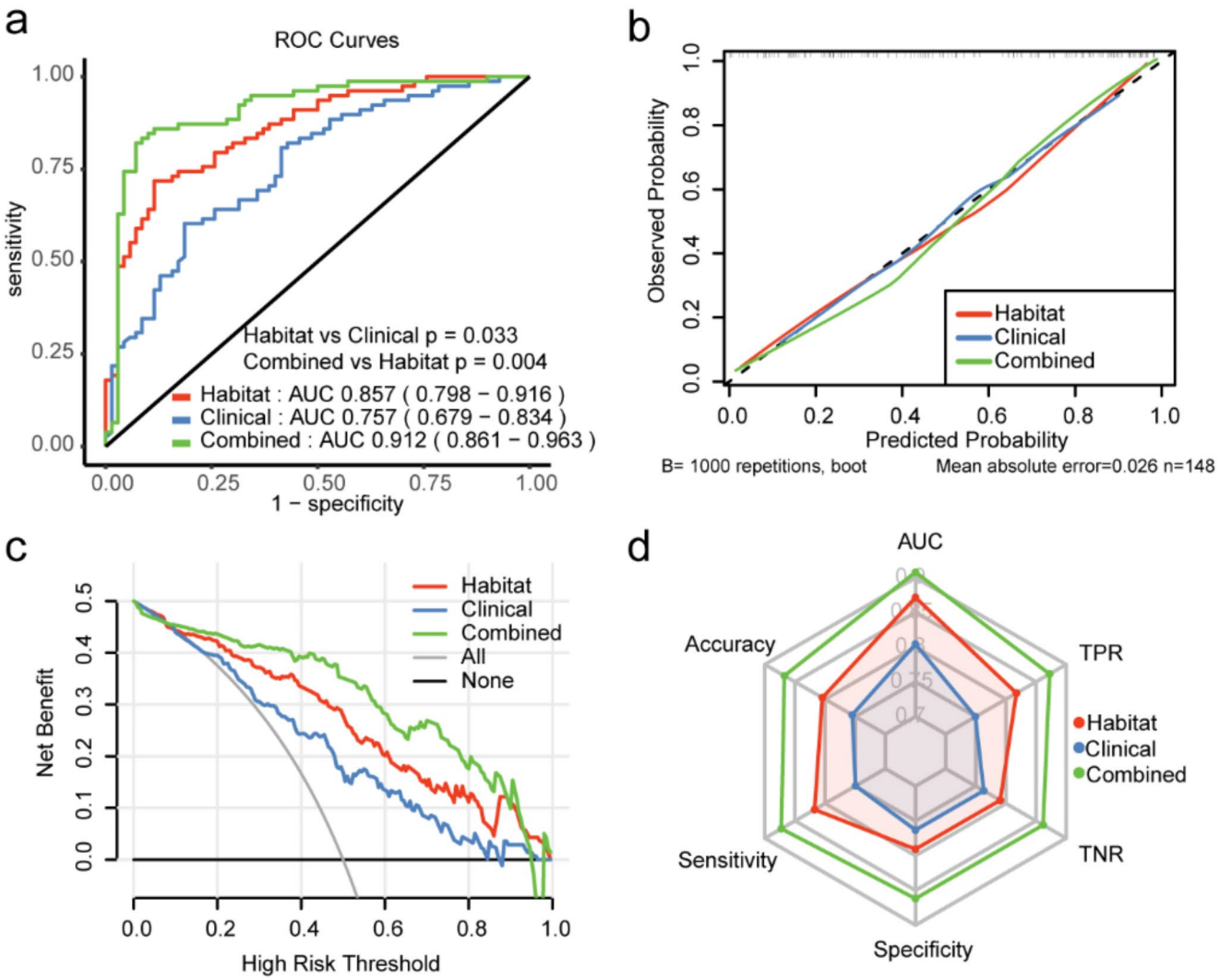

Fig. 6 Performance evaluation and comparison of the models for predicting the therapeutic response of HAIC-FOLFOX treatment. Receiver operator characteristic (ROC) curves (**a**); Calibration curves (**b**); Decision curves (**c**); Radar chart (**d**) shows comparison of performance metrics across different models

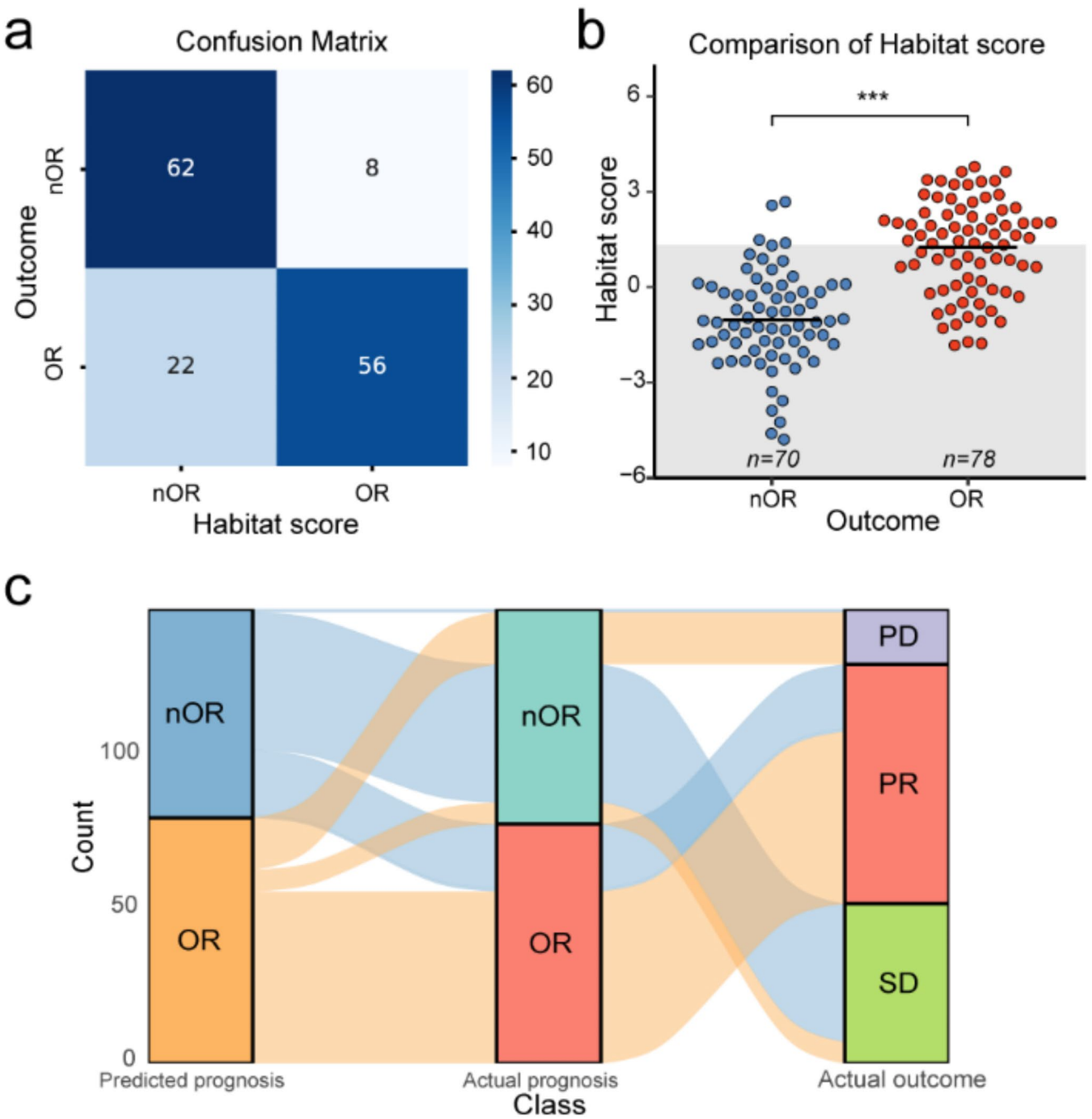

Fig. 7 Performance evaluation of the habitat radiomics model for predicting the therapeutic response of HAIC-FOLFOX treatment. (**a**) Confusion matrix; (**b**) (**c**) Distributions of habitat radiomics model scores in OR groups and non-OR groups; (**c**) Alluvial diagram for predicting HAIC-FOLFOX treatment response using habitat radiomics model

4 Discussion

For HCC, the high tumor heterogeneity and complex tumor microenvironment lead to significant variability in response to HAIC-FOLFOX treatment [21]. Therefore, assessing tumor heterogeneity and predicting treatment response before formulating a treatment plan is particularly important. Several studies have shown that habitat radiomics, which quantifies tumor spatial heterogeneity, offers unique advantages and outperforms traditional radiomics in predicting tumor treatment response [22, 23]. In this study, we first developed and validated a CECT-based habitat radiomics model for predicting the early therapeutic response to HAIC-FOLFOX in patients with unresectable HCC. The

habitat radiomics model showed outstanding predictive ability and could also accurately stratify patients into two prognostic subgroups with significantly different responses, indicating that the model may be beneficial for personalized pretreatment decision-making.

According to the clustering analysis, the HCCs were encoded into three habitats (Habitat 1: low AE and low VE; Habitat 2: moderate AE and moderate VE; Habitat 3: high AE and high VE). We then quantify tumor spatial heterogeneity using a multiregional spatial interaction (MSI) matrix, grounded in the concept that 'interactions between tumor microenvironment components regulate and influence the biological characteristics of the tumor [24, 25], thereby impacting its treatment response.' In this approach, each voxel in the imaging data is considered the smallest unit, with interactions occurring between adjacent units. These interactions encapsulate biological information from the tumor microenvironment. The results indicate that 'habitat 1.1 (the proportion of habitat 1)', and 'b01 (the proportion of interaction between liver tissue and habitat 1)' are risk factors for an early radiographic response to HAIC-FOLFOX, while 'habitat 3.1 (the proportion of habitat 3)', '2b3r (the proportion of interaction between habitat 2 and habitat 3)', and '2border0 (the interaction intensity between habitat 2 and liver tissue)' are protective factors. Habitat 1 exhibited low AE and low VE. In contrast, Habitat 3 exhibited high AE and high VE, indicating that the high-risk habitat had a high proportion of low-enhancement areas. In contrast, the low-risk habitat had a high proportion of high-enhancement areas. These findings are consistent with the findings of Kim et al., who identified diffuse hyperenhancing HCC (more than 50% of the tumor area exhibits nonrimlike enhancement greater than that of the adjacent liver parenchyma) as a favorable prognostic factor for the HAIC-FOLFOX treatment outcome [26]. Base on the collected pathological data, tumors with a higher proportion of high-enhancement habitat show elevated expression levels of CD34 and CD31 (sFig. 3), highlighting increased angiogenesis. This is closely associated with the efficacy of vascular interventional therapy in HCC, as arterial hypervascularity in HCC patients was previously found to be significantly associated with improved outcomes after TACE [27, 28]. This may be explained by the fact that compared to tumors with fewer blood vessels, hypervascular HCCs exhibit a more sensitive response to TACE because of increased delivery and uptake of chemotherapeutic embolic agents. Given that HAIC-FOLFOX delivers chemotherapy drugs via the hepatic artery branches supplying the tumor, similar principles may apply. MRI research on HCC has reported that higher overall tumor perfusion (as described by the area under the curve of the gadolinium contrast agent concentration) can predict a favorable prognosis for HAIC-FOLFOX treatment, as it correlates with greater tissue delivery of drugs [29]. Additionally, the histopathological analysis suggests that tumors with a high proportion of highly enhanced habitat exhibit higher tumor cell differentiation, which corresponds to a histological subtype with a better prognosis. These tumors also show low Ki-67 expression, indicating lower tumor proliferation activity and a lower degree of malignancy (sFig. 3). In contrast, tumors with a high proportion of low- to moderate-enhancing habitat display poorer cell differentiation, higher nuclear atypia, and elevated Ki-67 expression, reflecting increased tumor proliferation and greater invasiveness. This observation is indirectly supported by studies reporting that macrotrabecular-massive HCC and vessels encapsulating tumor cluster patterns are associated with larger tumor diameters and intratumoral necrosis [30]. In low-perfusion habitats, which contain a significant portion of necrotic tumor areas, high-risk habitats may be correlated with these adverse pathological features of trabecular and massive HCC and vessels encompassing tumor clusters. High-risk habitats also exhibit characteristics such as a larger volume of interaction between low-enhancement subregions and liver tissue (b01). Studies have reported that the two-trait predictor of venous invasion (i.e., the presence of intratumoral arterial signal during the arterial phase and a hypodense halo around the tumor margin during the portal venous phase) is an independent risk factor for predicting microvascular invasion (MVI) in HCC patients [31]. The 'b01' feature may represent the habitat manifestation of the hypodense halo of the tumor margin, indicating the potential presence of MVI, which is an adverse prognostic pathological feature.

For clinical variables, logistic regression analysis revealed that comorbidities, cirrhosis, vascular invasion vp classification, and TBIL were independent risk factors for the response to HAIC-FOLFOX treatment. These risk factors have been previously reported in prognostic studies of HCC patients treated with HAIC [32, 33]. Comorbidities include diabetes, hypertension, and coronary artery disease, with diabetes and hypertension being the primary conditions. A substantial body of evidence indicates that diabetes itself worsens the prognosis of HCC, possibly due to endoplasmic reticulum stress and immune dysfunction [34, 35]. The clinical model demonstrated moderate predictive performance, which was primarily attributed to significant fluctuations in serum markers and interindividual differences.

Our study represents advancements in medical image analysis in several aspects. First, previous research has primarily focused on traditional radiomics, which often has difficulty providing direct biological interpretations. These approaches typically involve calculating the average of various numerical values from tumor ROIs, which may overlook information regarding the spatial distribution

heterogeneity of tumors. Second, research on habitat imaging has primarily focused on brain tumors and breast cancer, with limited attention given to liver cancer, which has a heavy disease burden. This is a gap in research that needs to be addressed to uncover new imaging biomarkers for HCC prognosis and provide more options for precision and personalized treatments. We conducted, for the first time in an HCC population, a habitat study based on CECT, exploring its relationship with the response to HAIC-FOLFOX treatment. Third, there is a significant gap in the identification of reliable biomarkers for predicting the efficacy of HAIC-FOLFOX. The habitat model demonstrated superior predictive performance, as evidenced by an AUC of 0.857 (95% CI 0.798–0.916), surpassing that of the ALBI grade combined with an MRI-based radiomics model (AUC: 0.79, 95% CI 0.68–0.90) [36] and the clinical nomogram that incorporates the tumor size, vascular invasion, metastasis, the albumin-bilirubin grade, and the alpha-fetoprotein level (C-index: 0.710–0.784) [32, 33, 37, 38].

In the present study, the majority of the patients received TKI and PD-1 inhibitor therapy. According to previous studies, the ORR of TKI and PD-1 inhibitor therapy varies from 23 to 34%, and the ORR of HAIC-FOLFOX combined with a TKI or PD-1 inhibitor varies from 48 to 76% [39–41]. Our study revealed that the ORR was 52.7% in patients treated with HAIC-FOLFOX combined with a TKI or PD-1 inhibitor, which was similar to previous studies, indicating that HAIC-FOLFOX plays a pivotal role in these cohorts. On the other hand, we focused on the early therapeutic response within 2 months post-HAIC treatment. In such a short time, the effect of TKI or PD-1 may remain obscure. Therefore, the HCC habitat radiomics model constructed in the present study is suitable for predicting the prognosis of patients treated with HAIC-FOLFOX.

This study has a few limitations. First, this was a retrospective study with a small sample size, and a large-scale prospective validation cohort is needed. Second, the risk of selection bias was unavoidable in this observational study. Third, we did not investigate the ability of the habitat model to predict overall survival (OS) or progression-free survival (PFS) in unresectable HCC patients. Thus, continued follow-up is highly valuable. Fourth, the potential impact of different CT scanners and parameters across the three centers on the model's performance.

5 Conclusions

In conclusion, we constructed, for the first time, a habitat radiomics model based on CECT to effectively and noninvasively predict the early therapeutic response of unresectable HCC patients to HAIC-FOLFOX treatment, which could guide clinical management and individual decision-making for patients with unresectable HCC.

Supplementary Information The online version contains supplementary material available at https://doi.org/10.1007/s13402-025-01041-0.

Author contributions M.W., Z.Q. and S.L. conceptualization, writing – original draft, writing – review & editing. G.L. and J.L. and Y.H. data curation, software. S.W. project administration, formal analysis, concepts and designs. X.L., N.Y. and L.W. supervision, project administration. All authors reviewed the manuscript.

Funding This work was supported by National Natural Science Foundation of China (NSFC: 82273484) and project of Chongqing young and middle-aged medical talents.

Data availability The datasets used and/or analysed during the current study are available from the corresponding author on reasonable request.

Declarations

Ethical approval The study received ethical approval from the ethics committees of Army Medical Center of PLA with approval number 2023 (280-01), the ethics committee of the First Affiliated Hospital of Chongqing Medical University, and medical ethics committees of Second Affiliated Hospital of Army Medical University of PLA.

Patient consent Informed consent was obtained in advance from all patients participating in the study, permitting the use of their medical records for this research and the publication of the study results in academic journals.

Competing interests The authors declare no competing interests.

Open Access This article is licensed under a Creative Commons Attribution-NonCommercial-NoDerivatives 4.0 International License, which permits any non-commercial use, sharing, distribution and reproduction in any medium or format, as long as you give appropriate credit to the original author(s) and the source, provide a link to the Creative Commons licence, and indicate if you modified the licensed material. You do not have permission under this licence to share adapted material derived from this article or parts of it. The images or other third party material in this article are included in the article's Creative Commons licence, unless indicated otherwise in a credit line to the material. If material is not included in the article's Creative Commons licence and your intended use is not permitted by statutory regulation or exceeds the permitted use, you will need to obtain permission directly from the copyright holder. To view a copy of this licence, visit http://creativecommons.org/licenses/by-nc-nd/4.0/.

References

1. H. Sung, J. Ferlay, R.L. Siegel, M. Laversanne, I. Soerjomataram, A. Jemal, F. Bray, CA Cancer J. Clin. **71**, 209–249 (2021). https://doi.org/10.3322/caac.21660
2. S. Roayaie, G. Jibara, P. Tabrizian, J.-W. Park, J. Yang, L. Yan, M. Schwartz, G. Han, F. Izzo, M. Chen, J.-F. Blanc, P. Johnson, M. Kudo, L.R. Roberts, M. Sherman, Hepatol. (Baltimore Md). **62**, 440–451 (2015). https://doi.org/10.1002/hep.27745

3. A. Vogel, A. Cervantes, I. Chau, B. Daniele, J.M. Llovet, T. Meyer, J.C. Nault, U. Neumann, J. Ricke, B. Sangro, P. Schirmacher, C. Verslype, C.J. Zech, D. Arnold, E. Martinelli, Ann. Oncol. **29**, iv238–iv255 (2018). https://doi.org/10.1093/annonc/mdy308
4. G. Cabibbo, M. Enea, M. Attanasio, J. Bruix, A. Craxì, C. Cammà, Hepatol. (Baltimore Md). **51**, 1274–1283 (2010). https://doi.org/10.1002/hep.23485
5. J.A. Marrero, L.M. Kulik, C.B. Sirlin, A.X. Zhu, R.S. Finn, M.M. Abecassis, L.R. Roberts, J.K. Heimbach, Hepatol. (Baltimore Md). **68**, 723–750 (2018). https://doi.org/10.1002/hep.29913
6. M. Pinter, B. Scheiner, M. Peck-Radosavljevic, Gut. **70**, 204–214 (2021). https://doi.org/10.1136/gutjnl-2020-321702
7. J.H. Choi, W.J. Chung, S.H. Bae, D.S. Song, M.J. Song, Y.S. Kim, H.J. Yim, Y.K. Jung, S.J. Suh, J.Y. Park, D.Y. Kim, S.U. Kim, S.B. Cho, Cancer Chemother. Pharmacol. **82**, 469–478 (2018). https://doi.org/10.1007/s00280-018-3638-0
8. M. Ikeda, S. Shimizu, T. Sato, M. Morimoto, Y. Kojima, Y. Inaba, A. Hagihara, M. Kudo, S. Nakamori, S. Kaneko, R. Sugimoto, T. Tahara, T. Ohmura, K. Yasui, K. Sato, H. Ishii, J. Furuse, T. Okusaka, Ann. Oncol. **27**, 2090–2096 (2016)
9. N. Lyu, Y. Kong, L. Mu, Y. Lin, J. Li, Y. Liu, Z. Zhang, L. Zheng, H. Deng, S. Li, Q. Xie, R. Guo, M. Shi, L. Xu, X. Cai, P. Wu, M. Zhao, J. Hepatol. **69**, 60–69 (2018). https://doi.org/10.1016/j.jhep.2018.02.008
10. M. He, Q. Li, R. Zou, J. Shen, W. Fang, G. Tan, Y. Zhou, X. Wu, L. Xu, W. Wei, Y. Le, Z. Zhou, M. Zhao, Y. Guo, R. Guo, M. Chen, M. Shi, JAMA Oncol. **5**, 953–960 (2019). https://doi.org/10.1001/jamaoncol.2019.0250
11. Q.J. Li, M.K. He, H.W. Chen, W.Q. Fang, Y.M. Zhou, L. Xu, W. Wei, Y.J. Zhang, Y. Guo, R.P. Guo, M.S. Chen, M. Shi, J. Clin. Oncol. **40**, 150–160 (2022). https://doi.org/10.1200/jco.21.00608
12. M.R. Junttila, F.J. de Sauvage, Nature. **501**, 346–354 (2013). https://doi.org/10.1038/nature12626
13. E. Sala, E. Mema, Y. Himoto, H. Veeraraghavan, J.D. Brenton, A. Snyder, B. Weigelt, H.A. Vargas, Clin. Radiol. **72** (2017). https://doi.org/10.1016/j.crad.2016.09.013
14. J. Wu, G. Cao, X. Sun, J. Lee, D.L. Rubin, S. Napel, A.W. Kurian, B.L. Daniel, R. Li, Radiology. **288**, 26–35 (2018). https://doi.org/10.1148/radiol.2018172462
15. J. Li, Z. Qiu, C. Zhang, S. Chen, M. Wang, Q. Meng, H. Lu, L. Wei, H. Lv, W. Zhong, X. Zhang, Eur. Radiol. **33**, 893–903 (2023). https://doi.org/10.1007/s00330-022-09055-0
16. P. Wen, S.D. Chen, J.R. Wang, Y.H. Zeng, Oncol. Res. **27**, 583–592 (2019). https://doi.org/10.3727/096504018x15368325811545
17. B.K. Kim, S.U. Kim, K.A. Kim, Y.E. Chung, M.J. Kim, M.S. Park, J.Y. Park, D.Y. Kim, S.H. Ahn, M.D. Kim, S.I. Park, J.Y. Won, D.Y. Lee, K.H. Han, J. Hepatol. **62**, 1304–1310 (2015). https://doi.org/10.1016/j.jhep.2015.01.022
18. R. Lencioni, J.M. Llovet, Semin Liver Dis. **30**, 52–60 (2010). https://doi.org/10.1055/s-0030-1247132
19. T.-Y. Xia, Z.-H. Zhou, X.-P. Meng, J.-H. Zha, Q. Yu, W.-L. Wang, Y. Song, Y.-C. Wang, T.-Y. Tang, J. Xu, T. Zhang, X.-Y. Long, Y. Liang, W.-B. Xiao, S.-H. Ju, Radiology. **307** (2023). https://doi.org/10.1148/radiol.222729. e222729
20. J.E. Park, H.S. Kim, N. Kim, S.Y. Park, Y.-H. Kim, J.H. Kim, Clin. Cancer Res. **27**, 237–245 (2021). https://doi.org/10.1158/1078-0432.CCR-20-2156
21. X. Yang, C. Yang, S. Zhang, H. Geng, A.X. Zhu, R. Bernards, W. Qin, J. Fan, C. Wang, Q. Gao, Cancer Cell. **42**, 180–197 (2024). https://doi.org/10.1016/j.ccell.2024.01.007
22. J. Peng, D. Zou, X. Zhang, H. Ma, L. Han, B. Yao, J. Transl Med. **22**, 87 (2024). https://doi.org/10.1186/s12967-024-04904-6
23. J. Wu, M.F. Gensheimer, N. Zhang, M. Guo, R. Liang, C. Zhang, N. Fischbein, E.L. Pollom, B. Beadle, Q.-T. Le, R. Li, J. Nucl. Med. **61**, 327–336 (2020). https://doi.org/10.2967/jnumed.119.230037
24. Y. Chen, S. Liu, S. Tan, Y. Zheng, Y. Chen, C. Yang, S. Lin, Y. Mi, W. Li, Gut Microbes. **16**, 2423043 (2024). https://doi.org/10.1080/19490976.2024.2423043
25. Y. Chen, Y. Zheng, S. Liu, J Cell Mol Med. **28**, e70182 (2024). https://doi.org/10.1111/jcmm.70182
26. B. Kim, J.H. Won, J. Kim, Y. Kwon, H.J. Cho, J. Huh, J.K. Kim, AJR Am. J. Roentgenol. **216**, 1566–1573 (2021). https://doi.org/10.2214/AJR.20.23213
27. S. Katyal, J.H. Oliver, M.S. Peterson, P.J. Chang, R.L. Baron, B.I. Carr, AJR Am. J. Roentgenol. **175**, 1665–1672 (2000)
28. J.H. Kim, H.-K. Yoon, G.-Y. Ko, D.I. Gwon, C.S. Jang, H.-Y. Song, J.H. Shin, K.-B. Sung, Radiology. **255**, 270–277 (2010). https://doi.org/10.1148/radiol.09091076
29. W.R. Jarnagin, L.H. Schwartz, D.H. Gultekin, M. Gönen, D. Haviland, J. Shia, M. D'Angelica, Y. Fong, R. DeMatteo, A. Tse, L.H. Blumgart, N. Kemeny, Ann. Oncol. **20**, 1589–1595 (2009). https://doi.org/10.1093/annonc/mdp029
30. Z. Feng, H. Li, H. Zhao, Y. Jiang, Q. Liu, Q. Chen, W. Wang, P. Rong, Radiology. **300**, 219–229 (2021). https://doi.org/10.1148/radiol.2021203614
31. M. Renzulli, S. Brocchi, A. Cucchetti, F. Mazzotti, C. Mosconi, C. Sportoletti, G. Brandi, A.D. Pinna, R. Golfieri, Radiology. **279**, 432–442 (2016). https://doi.org/10.1148/radiol.2015150998
32. W. Yao, R. Wei, J. Jia, W. Li, M. Zuo, S. Zhuo, G. Shi, P. Wu, C. An, Ther. Adv. Med. Oncol. **15**, 17588359231163845 (2023). https://doi.org/10.1177/17588359231163845
33. J. Mei, W.-P. Lin, F. Shi, W. Wei, J.-B. Liang, M. Shi, L. Zheng, S.-H. Li, R.-P. Guo, Eur. J. Radiol. **142**, 109890 (2021). https://doi.org/10.1016/j.ejrad.2021.109890
34. T. Nakatsuka, R. Tateishi, Clin. Mol. Hepatol. **29**, 51–64 (2023). https://doi.org/10.3350/cmh.2022.0095
35. W.-S. Yang, P. Va, F. Bray, S. Gao, J. Gao, H.-L. Li, Y.-B. Xiang, PLoS One. **6**, e27326 (2011). https://doi.org/10.1371/journal.pone.0027326
36. Y. Zhao, F. Huang, S. Liu, L. Jian, X. Xia, H. Lin, J. Liu, J. Cancer Res. Clin. Oncol. **149**, 5181–5192 (2023). https://doi.org/10.1007/s00432-022-04467-3
37. B. Liu, S. Gao, J. Guo, F. Kou, S. Liu, X. Zhang, X. Wang, G. Cao, H. Chen, P. Liu, H. Xu, Q. Gao, R. Yang, X. Zhu, Transl Oncol. **34**, 101705 (2023). https://doi.org/10.1016/j.tranon.2023.101705
38. M. Deng, Q. Lei, J. Wang, C. Lee, R. Guan, S. Li, W. Wei, H. Chen, C. Zhong, R. Guo, Int. J. Surg. **109**, 1299–1310 (2023). https://doi.org/10.1097/JS9.0000000000000376
39. X. Chang, X. Li, P. Sun, Z. Li, P. Sun, S. Ning, BMC Cancer. **24**, 480 (2024). https://doi.org/10.1186/s12885-024-12233-6
40. L. Diao, C. Wang, R. You, B. Leng, Z. Yu, Q. Xu, Y. Cheng, G. Yin, J. Gastroenterol. Hepatol. **39**, 746–753 (2024). https://doi.org/10.1111/jgh.16463
41. Y. Pan, R. Wang, D. Hu, W. Xie, Y. Fu, J. Hou, L. Xu, Y. Zhang, M. Chen, Z. Zhou, Front. Biosci. (Landmark Ed). **26**, 873–881 (2021). https://doi.org/10.52586/4994

Publisher's note Springer Nature remains neutral with regard to jurisdictional claims in published maps and institutional affiliations.

Authors and Affiliations

Mingsong Wu[1] · Zenglong Que[2] · Shujie Lai[1] · Guanhui Li[1] · Jie Long[1] · Yuqin He[1] · Shunan Wang[3] · Hao Wu[4] · Nan You[5] · Xiang Lan[6] · Liangzhi Wen[1]

✉ Nan You
younan@tmmu.edu.cn

✉ Xiang Lan
lanxiang_tmmu@163.com

✉ Liangzhi Wen
wenliangzhi@tmmu.edu.cn

Mingsong Wu
wumingsong@tmmu.edu.cn

Zenglong Que
qzl960yy@163.com

Shujie Lai
laisj130@tmmu.edu.cn

Guanhui Li
liguanhui@tmmu.edu.cn

Jie Long
longjie@tmmu.edu.cn

Yuqin He
hyq1988@tmmu.edu.cn

Shunan Wang
wangshunan@tmmu.edu.cn

Hao Wu
cefradine1005@gmail.com

[1] Department of Gastroenterology, Daping Hospital, Army Medical University (Third Military Medical University), No. 10, Changjiang Branch Road, Yuzhong District, Chongqing 400042, P. R. China

[2] Department of Infectious Diseases, The 960 Hospital of PLA, No. 25, Shifan Road, Tianqiao District, Jinan City, Shandong Province 250031, P. R. China

[3] Department of Radiological, Daping Hospital, Army Medical University (Third Military Medical University), No. 10, Changjiang Branch Road, Yuzhong District, Chongqing 400042, P. R. China

[4] Department of Radiological, The First Affiliated Hospital of Chongqing Medical University, No. 1 Youyi Road, Yuanjiagang, Yuzhong District, Chongqing 400042, P. R. China

[5] Department of Hepatobiliary, Xinqiao Hospital Affiliated to The Army Medical University, No. 1 Xinqiao Main Street, Shapingba District, Chongqing 400037, P. R. China

[6] Department of Hepatobiliary, The First Affiliated Hospital of Chongqing Medical University, No. 1 Youyi Road, Yuanjiagang, Yuzhong District, Chongqing 400042, P. R. China